JOURNAL OF PROPULSION AND POWER
Vol. 15, No. 1, January–February 1999

Performance Computation of a Low-Power Hydrogen Arcjet

Kazuhisa Fujita* and Yoshihiro Arakawa†
University of Tokyo, Tokyo 113, Japan

A numerical analysis of a low-power hydrogen arcjet has been conducted by taking account of the chemical and thermal nonequilibria by separating the electron temperature from the heavy species temperature. A sheath model is introduced to the electrode boundaries to evaluate the electrode potential drops in a coupled manner with the flow calculation. Comparison of calculated performance for the IRS ARTUS-4 thruster with experimental results shows good agreement regarding the discharge voltage and specific impulses, although the heat loss is somewhat underestimated. To account for these discrepancies, the radiative loss is computed in detail, taking account of the bound–bound, free–bound, and free–free electronic transitions in the hydrogen plasma. The estimated radiation is found to become significant as the electron temperature exceeds approximately 12,000 K. Contribution of the radiative heat transfer to the total heat loss is discussed briefly. The results suggest that the radiation analysis may be necessary for further accurate prediction of thruster performance, even under low-power operation.

Nomenclature

D = diffusion coefficient
e = elementary charge
I = total current
j = current density
k_B = Boltzmann's constant
m = mass of particle
$\dot{m}$ = propellant mass flow rate
N = thermionic emission rate
n = number density of particles
r = coordinate normal to electrode surface
S = rate of ionization in sheath
T = temperature, or thrust
V = discharge voltage
ε_i = ionization potential
κ = thermal conductivity
ν^m = momentum-transfer collision frequency
σ = electrical conductivity
ϕ = electric potential

Subscripts
A = ambipolar diffusion
a, m = atomic and molecular hydrogen, respectively
d = electrode sheath edge
e = electron
g = heavy species
i = ion, or ionization
j = running index of species
n = neutral
0 = electrode surface

Introduction

RECENTLY, interest in arcjets has increased because of their promising features for primary propulsion functions.[1–3] Up to now, low-power arcjets have achieved a high degree of qualification, and recent arcjet research has been directed to extension of the operating envelope to a higher specific impulse and efficiency. To accomplish this, it is necessary to improve our understanding of arcjet physics, and then to build reliable models that can help design arcjets of the next generation.

Numerical simulations of arcjet operation have become more realistic[4–6] because of the recent remarkable improvements in computer performance. The latest Megli-Krier-Burton model[7] successfully treats the highly complicated physics governing arcjet flow, where the two-temperature and non-Maxwellian distribution effects are investigated in detail. It is of primary importance for the numerical models to predict the arc behavior without any artificial boundary conditions imposed on the electric field boundaries, if one wants to predict the overall thruster performance self-consistently. The arc behavior is determined by the speed of arc growth in the radial direction compared with the axial flow velocity, which is subject to the nonequilibrium effects, namely the electron production rate, radial ambipolar diffusion, and the electron temperature deflection from the heavy species temperature.

In the present study, the chemical and thermal nonequilibria, in which the electron temperature is separated from the heavy species temperature, are incorporated into the numerical model (two-temperature model). A sheath model is proposed and applied to the electrode boundaries to determine the boundary values of the plasma property and the electrode potential drops. Numerical simulations of the IRS ARTUS-4 thruster[8] are compared with the experimental results. A further accurate analysis of the radiation phenomena is conducted to account for underestimation of the heat loss found in the numerical predictions.

Low-Power Arcjet Model

Flow and Electric Field Model

The arcjet model consists of a set of the fluid-dynamic equations and the electric-field model, whose descriptions are given in Ref. 9 in detail. Fluid-dynamic phenomena are described by the Navier–Stokes equations in the cylindrical coordinates in which the z coordinate is aligned with the thruster axis. An azimuthal change of the physical property is neglected; however, the azimuthal components are accurately formulated so that swirl injection can be incorporated. Chemical nonequilibrium is taken into consideration, and the electron temperature is separated from the heavy species temperature (two-temperature model). On the other hand, an elliptic partial differential

Received June 2, 1997; revision received Feb. 13, 1998; accepted for publication June 17, 1998.

*JSPS Research Fellow, Department of Aeronautics and Astronautics, 7-3-1 Hongo, Bunkyo-ku; currently Research Associate, Institute of Space and Astronautical Science, 3-1-1 Yoshinodai, Sagamihara, Kanagawa 229, Japan. Member AIAA.

†Professor, Department of Aeronautics and Astronautics, 7-3-1 Hongo, Bunkyo-ku. Senior Member AIAA.

equation is used to determine the electric potential inside the arcjet, from which current and the Ohmic heating rate is evaluated by the generalized Ohm's law. Effects of the magnetic field on mobility of charged particles are neglected because the hall parameter is generally less than unity in the low-power arcjet.

Neglect of the self-induced magnetic field becomes inaccurate with increasing current or power. An excessive decrease of the propellant mass flow rate increases the hall parameter because particle collision frequencies decrease accordingly. From these facts, the model application is limited to the input power, the current, and the specific power less than 10 kW, 100 A, and 500 MJ/kg, respectively. In addition, the plenum pressure should be higher than 10 kPa to maintain the validity of the two-temperature and Maxwellian distribution assumptions used to evaluate the transport properties and the chemical reaction rates.

Electrode Sheath Model

An electrode sheath model is developed to determine the number densities of the charged species, the electron temperature, and the electric potential at the sheath edge, which are given to the flow and electric field equations as the boundary values. Figure 1 shows the schematic of the cathode sheath. The sheath is assumed to be one dimensional because of the small sheath thickness in the plasma under consideration.

Electrons reaching the sheath edge are the sum of those emitted thermally from the unit area of the cathode surface at a rate N as a function of the cathode temperature, and those produced by ionization at a rate S per unit area of the sheath envelope, whereas those having higher thermal energy than the potential barrier are lost to the cathode surface. Therefore, the electron flux at the sheath edge is given by

$$\frac{j_{e_d}}{e} = n_d \sqrt{\frac{k_B T_{e_d}}{2\pi m_e}} \exp\left(\frac{e\phi_0}{k_B T_{e_d}}\right) - N - S \tag{1}$$

The thermionic emission rate is approximated by the Richardson–Dushman equation:

$$N = AT_0^2 \exp\left(-\frac{e\phi_W}{k_B T_0}\right) \tag{2}$$

where values of A and ϕ_W are taken from Ref. 10. Properly speaking, numerous calculations of phenomena inside the sheath are necessary to obtain the ionization rate; however, such an approach is unfavorable for computation of the entire arcjet flow. Therefore, we propose an approximated semiempirical formula, which is derived by assuming the averaged number densities and kinetic energy of particles, and the constant electric field in the sheath:

$$S = \gamma N n_n \sqrt{\frac{T_0 T_{e_d}}{n_d}} \exp\left(\frac{\varepsilon_i}{e\phi_0}\right) \tag{3}$$

where n_n is the number density of neutrals on the cathode surface, and γ is a coefficient related to the corresponding ionization cross section, which is numerically evaluated in the present study for hydrogen as

$$\gamma = 1.94 \times 10^{-15},\ \mathrm{m^{3/2}\ K^{-1}} \tag{4}$$

On the other hand, ions reach the sheath edge from the plasma with a velocity corresponding to the presheath potential at the order of the electron temperature in the plasma. Additionally, the total ion flux here is equivalent to the ambipolar diffusion flux from the plasma

$$\frac{j_{i_d}}{e} = -n_d \sqrt{\frac{2k_B T_{e_d}}{m_i}} = \frac{j_{A_d}}{e} \tag{5}$$

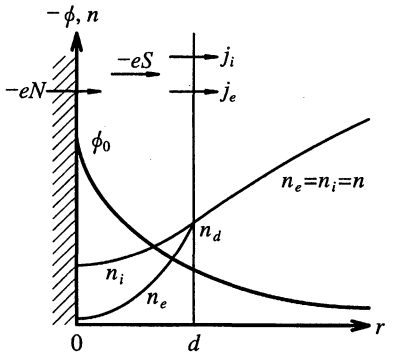

Fig. 1 Schematic of cathode sheath.

where

$$\frac{j_{A_d}}{e} = -\left(D_A \frac{\partial n}{\partial r}\right)_d \tag{6}$$

On the sheath edge, the total current density is given by $j_d = j_{i_d} + j_{e_d}$. Insertion of Eqs. (1) and (5) with Eq. (3) into this equation yields

$$j_d = \left[1 - \sqrt{\frac{m_i}{4\pi m_e}} \exp\left(\frac{e\phi_0}{k_B T_{e_d}}\right)\right] j_{A_d} - \left[1 + \gamma n_n \sqrt{\frac{T_0 T_{e_d}}{n_d}} \exp\left(\frac{\varepsilon_i}{e\phi_0}\right)\right] eN \tag{7}$$

Shown in Fig. 2 are the characteristics of the cathode potential drop vs surface temperature calculated by Eq. (7) for typical hydrogen operation with W–ThO_2 as the cathode material. A decrease in cathode surface temperature is found to decrease the potential drop. This is because the ionization rate in the sheath should be increased by decreasing the potential drop to maintain the current density. An increase of the neutral number density conversely increases the potential drop, because production of the charged particles can be correspondingly increased in the sheath.

The electron temperature at the sheath edge is associated with the potential drop and the electron heat conduction from the plasma. The latter should be equal to the heat flux brought to the cathode by a fraction of electrons reaching the cathode surface:

$$\left(-\kappa_e \frac{\partial T_e}{\partial r}\right)_d = \frac{n_d (k_B T_{e_d})^{3/2}}{\sqrt{2\pi m_e}} \left(2 - \frac{e\phi_0}{k_B T_{e_d}}\right) \exp\left(\frac{e\phi_0}{k_B T_{e_d}}\right) \tag{8}$$

Finally, Eqs. (5), (7), and (8) form consistent nonlinear simultaneous equations for n_d, T_{e_d}, and ϕ_0. The current density j_d is given from the electric field calculation. Because j_{A_d} and $(-\kappa_e \partial T_e/\partial r)_d$ are also connected with boundary values, the simultaneous equations are solved iteratively.

The sheath model can apply to the anode in a similar sense, though the signs are somewhat different. In this case, we can approximately neglect the thermionic emission and ionization in comparison with the diffusion flux, letting $N = \gamma = 0$ in Eq. (7).

Transport Properties

All of the transport properties are formulated in terms of the collision frequency, which is defined as a function of the temperature and the number density of the target species. When the collision cross section is available, the corresponding collision frequency is evaluated by numerical integration with the Maxwellian distribution for the incident velocity relative to the targets, and then expressed as a curve-fit function of the tem-

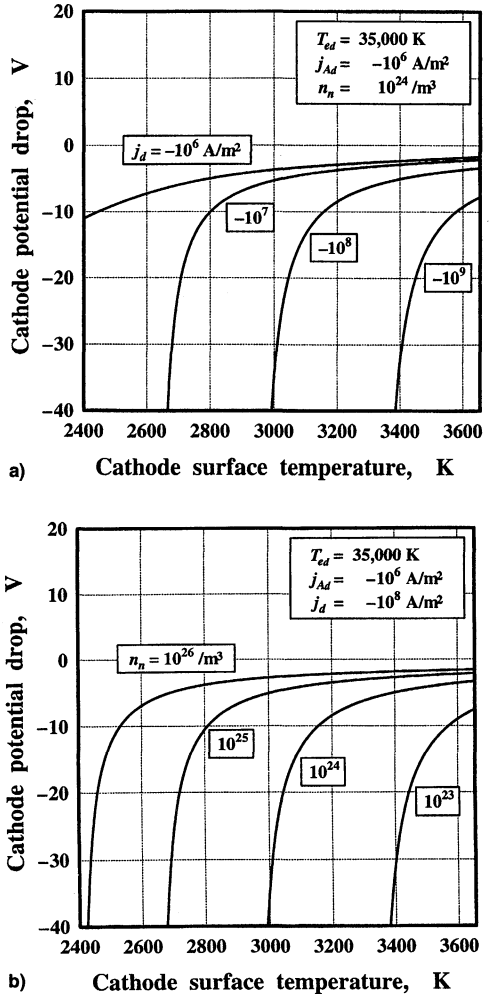

Fig. 2 Cathode potential drop vs surface temperature with variation of a) current density and b) neutral number density.

peratures.[11] If the collision integral is available, it is directly used to describe the frequency. On the other hand, the collision frequency whose cross section is not available is conversely derived from the diffusion coefficient, viscosity, mobility, or conductivity, which is evaluated experimentally or theoretically.

The electrical conductivity is defined by neglecting the ion current as

$$\sigma = n_e e^2 \Big/ m_e \sum_j \nu_{ej}^m \tag{9}$$

The diffusion coefficient and thermal conductivity of heavy species j are formulated in a similar sense by summing up all of the collision frequencies for j. The viscosity of the whole fluid is defined by using the mixing rule in addition. The diffusion of ions is approximated by ambipolar diffusion with a coefficient defined by $D_A = (1 + T_e/T_g)D_i$.

Electrons undergo elastic and inelastic collisions with heavy particles, through which their translational energy is transferred to the heavy species. In collisions where an electron ionizes and dissociates a heavy particle, it is assumed that the energy corresponding to the ionization and dissociation energy is lost from the total energy of the electron gas, respectively. In collisions involving production or recombination of electrons, it is assumed that the electron thermal energy corresponding to the electron temperature is produced or lost, respectively. Concerning other collisions, the energy transfer rate is described in terms of the energy transfer collision frequencies.

Boundary Conditions

At the inlet boundary, the propellant mass flow rate and the injecting direction with a swirling component are specified as the operating parameters, and the stagnation temperature is given as 300 K. The inlet pressure is evaluated by first-order extrapolation because of the subsonic inflow to the arcjet. The mass concentration of the secondary species such as ions and dissociated species is set to zero. The electron temperature, which has thereby no physical meaning on this boundary, is set equal to the heavy species temperature to avoid numerical problems. At the nozzle exit, all independent variables are extrapolated from the upwind area because of the supersonic outflow at the exit. The subsonic flow in the boundary layer is found to have little influence on the entire flow characteristics.

On the electrode boundaries, the velocity and a normal gradient of pressure are set zero. The electron temperature and the mass concentration of charged particles are evaluated by the electrode sheath model described earlier. Regarding other species, the electrode surface is accepted as the flow boundary, on which thermal equilibrium is assumed. The heavy species temperature is set equal to the electrode surface temperature, and the mass concentration of the neutral species is evaluated by the Saha equation. The calculated composition is usually close to that obtained for the catalytic walls. On the center axis, the axisymmetric condition is used.

The discharge voltage is imposed as the cathode surface potential by a negative value with respect to the anode, and controlled iteratively so that the calculated total current can be equal to the desired value. Boundary values of the elliptic partial differential equation for the electric potential are given by adding the absolute value of the potential drop to the electrode surface potential. On the inlet, center axis, and nozzle exit boundaries, the electric field vector is directed tangentially to the boundaries.

Performance Computation of ARTUS-4

Performance calculation is conducted on the Nozzle-1 configuration of the IRS ARTUS-4 thruster,[8] operated at the 1.5-kW level using hydrogen as the propellant. The electrode geometry of Nozzle-1 is shown next. Constrictor diameter = 0.6 mm, constrictor length = 0.6 mm, half-angle of plenum chamber = 30 deg, half-angle of divergent nozzle = 20 deg, half-angle of cathode tip = 22.5 deg, cathode tip radius = 0.1 mm, and electrode gap = 0.8 mm. The area ratio of the divergent nozzle is 400. The inlet boundary of the computational domain is located 3.6 mm upstream from the cathode tip, where the conical part of the cathode begins, whereas the exit boundary is set to the nozzle exit. The grid contains 160-axial by 35-radial nodes, with grid concentrations to resolve the steep gradients of physical properties. The maximum temperatures of the anode and cathode surface are given by 2400 and 3200 K at the downstream end of the constrictor and at the cathode tip, respectively, whereas the minimum temperature is set 600 K at the inlet and exit points of the electrodes. Between the minimum and maximum points, the wall temperature distribution is given by linear interpolation, and kept constant through the calculation. The direction of swirl injection is set to 30 deg, with respect to the streamwise direction.

Chemistry of Hydrogen Propellant

Major chemical species in the low-power hydrogen arcjet are H_2, H, H^+, and e. Although a small number of molecular ions may exist, they are assumed to have little effect on the arc discharge. Major chemical reactions for this four-species system are presented in Table 1. The reaction rate coefficient is described as a product of the particle number densities and the Arrhenius-type function of the corresponding temperatures. A detailed description of the hydrogen chemical model and references are given in Ref. 11.

The free-bound radiative loss is incorporated in such a way that the electron thermal energy plus ionization energy is equal

Table 1 Chemical reaction model

Reaction	Reaction rate,[a] $k = AT^B \exp(-C/T)$		
	A	B	C
(1) $H_2 + e \rightarrow H + H + e$	7.0×10^{-16}	0.33	103,900
(2) $H_2 + B^b \rightarrow H + H + B$	9.1×10^{-12}	−1.0	51,900
(3) $H_2 + e \rightarrow H^+ + H + e + e$	5.9×10^{-17}	0.52	179,000
(4) $H + e \rightarrow H^+ + e + e$	2.5×10^{-17}	0.57	158,000
(5) $H + B \rightarrow H^+ + B + e$	3.3×10^{-19}	0.50	158,000
(6) $H + H + B \rightarrow H_2 + B$	5.0×10^{-42}	−1.0	0
(7) $H^+ + B + e \rightarrow H + B + h\nu$	2.0×10^{-14}	1.0	0
(8) $H^+ + e + e \rightarrow H + e + h\nu$	1.1×10^{-20}	−4.5	0

[a] k is expressed in $m^3\ s^{-1}$ or $m^6\ s^{-1}$, and T is T_g or T_e in K according to reactions.
[b] B is H_2, H, and H^+, and $h\nu$ represents a photon.

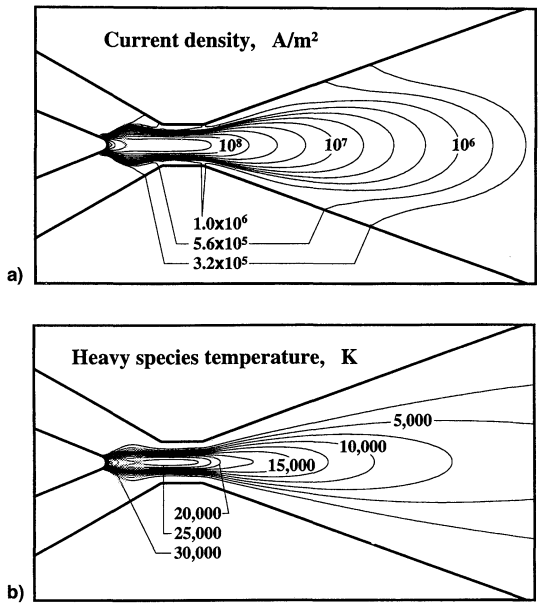

Fig. 3 Distributions of a) current density and b) heavy species temperature for $\dot{m}$ = 10 mg/s and I = 15 A.

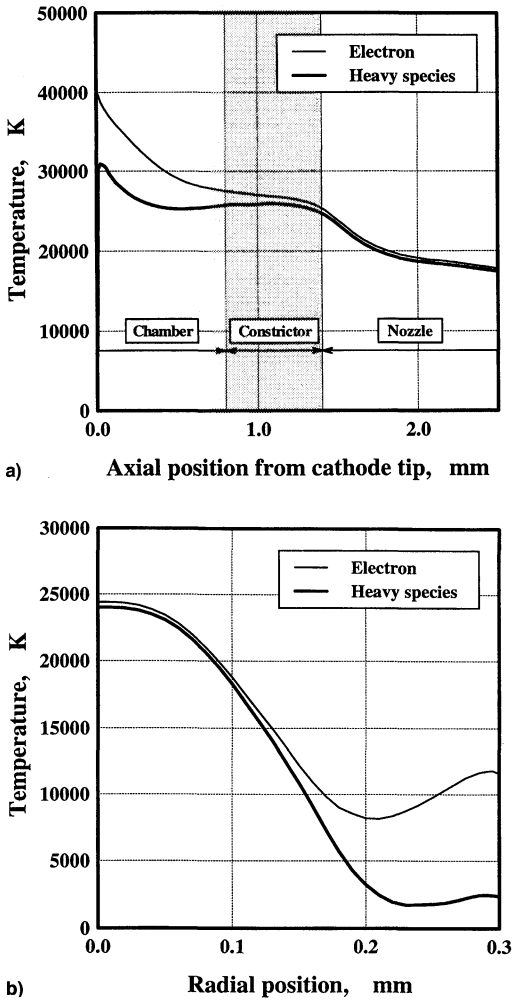

Fig. 4 Axial and radial profiles of electron and heavy species temperatures a) along the center axis and b) at the downstream end of constrictor, respectively, for $\dot{m}$ = 10 mg/s and I = 15 A.

to the radiation energy emitted in reactions (7) and (8). The free–free radiation (bremsstrahlung) is also taken into account with the Gaunt factor averaged for electrons having the Maxwellian velocity distribution.

Numerical Procedure

At the beginning of each iterative step, transport properties are first determined from results of the last step. The electric potential equation is then solved by the finite element method, from which the current and Ohmic heating rate are determined. The fluid-dynamic equations are then computed using a fully implicit time-marching technique to reduce the total computation time and numerical instability. The explicit terms are calculated by the symmetric Yee scheme,[12] whereas the implicit operators are constructed in the LU–ADI algorithm.[13] The source terms related with chemical reactions are linearized for time and treated implicitly to reduce numerical instability. Using implicit operation for the fluid-dynamic and chemical terms, we can accelerate time integration of the system equation by the factor of 4 in general, and more than 10 at the beginning of each calculation, in comparison with fully explicit computation. The boundary values are finally updated according to the boundary conditions. The nonlinear simultaneous equations of the electrode sheath model are solved iteratively by the Newton–Raphson method.

Results

Figure 3 shows typical contours of the current density and the heavy species temperature for $\dot{m}$ = 10.0 mg/s and I = 15.0 A. Current is found broadly distributed to the downstream area of the constrictor and the nozzle; however, a small portion of current is conducted to the upstream region. The arc column is constricted radially because of a high plenum pressure, and the propellant stream is channelled well in the constrictor, which reduces the heat conduction to the constrictor surface from the arc because of the cold gas envelope with low conductivity.

Axial and radial profiles of electron and heavy species temperatures are shown in Fig. 4. Both temperatures are found closely equilibrated in the arc column; however, they become uncoupled near the anode wall. Such a trend, which is also reported in Refs. 5–7, is a result of a decrease of the electron

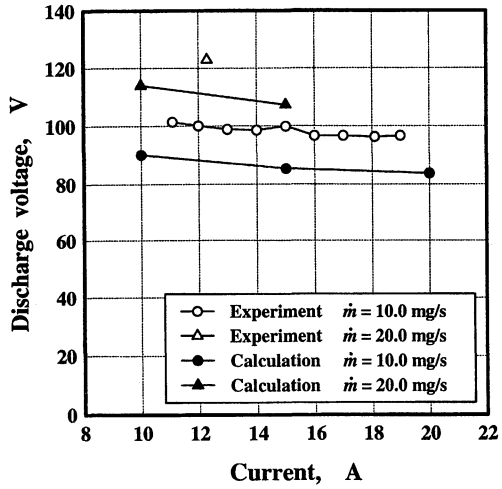

Fig. 5 Discharge voltage vs current.

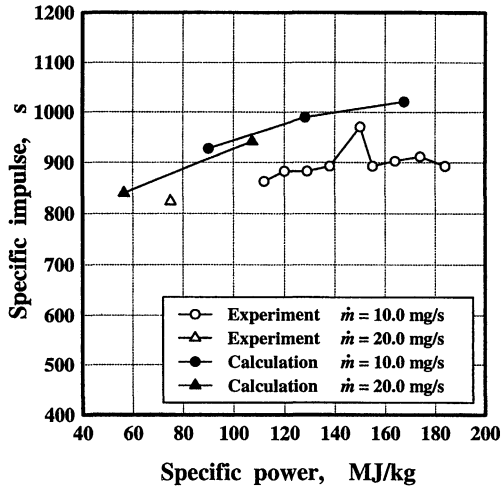

Fig. 6 Specific impulse vs specific power.

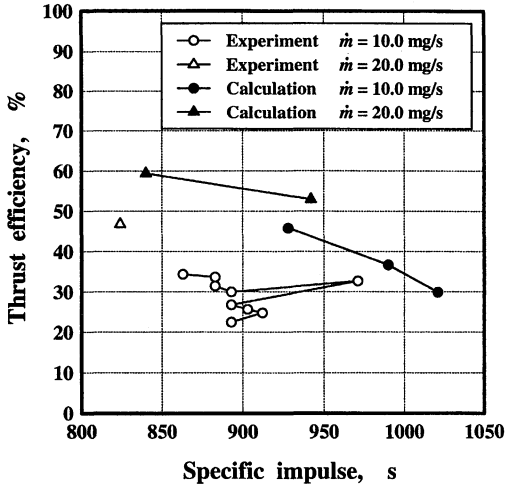

Fig. 7 Thrust efficiency vs specific impulse.

number density near the anode surface. Because the electron temperature does not decrease quickly along with the heavy species temperature in this region, the electron mobility remains large enough to maintain the arc discharge. The loose coupling of temperatures upstream of the constrictor is also a result of a decrease of the electron number density, because the arc is not well constricted here, and the flow is not yet sufficiently ionized in the upstream region.

Table 2 Energy distribution of arcjet flow for $\dot{m}$ = 20 mg/s and I = 10 A

Energy state	% of calculated IV[a]
Thermal	11.8
Dissociation	11.1
Ionization	4.3
Axial kinetic (thrust)	58.6
Radial kinetic	1.0
Azimuthal kinetic	0.1
Convective loss[b]	18.6
Radiative loss[b]	1.5

[a]Sum is 7% larger than IV because of numerical errors.
[b]Integrated values through the flow channel to the nozzle exit.

Numerical predictions are finally compared with the experimental values in Ref. 8. As plotted in Fig. 5, the calculated discharge voltages agree well with the experimental ones, though they are 10–15% lower. In contrast, the calculated thrust is 5–15% higher than the experiment, which leads to overestimation of the specific impulse as seen in Fig. 6. Because the thrust efficiency is defined by $\eta = T^2/2\dot{m}IV$, the overestimation of thrust and the underestimation of the discharge voltage deflect the predicted thrust efficiencies from the experimental values, as seen in Fig. 7.

One reason for this voltage discrepancy is the small magnitude of $|\phi_0|$, which is calculated typically to be 7–10 V at the cathode tip, whereas $|\phi_0|$ is generally less than 5 V at the anode arc attachment. This implies that more accurate treatment of interactions between the electrode and plasma flow than the present sheath model may be required. It may be necessary to incorporate an electrode thermal model with the flow, sheath, and electric field models to predict the arc attachment behavior more realistically.

The overestimation of thrust suggests that the energy distribution in the plasma flow is not sufficiently accurate. Table 2 shows a typical example of the final energy distribution evaluated at the nozzle exit. The reason for 7% error in the sum is that the grid is not optimized enough to eliminate numerical errors in current and energy conservation. A smaller amount of frozen-flow loss than that of Ref. 6 is partly because of the lower power. However, these results imply that the thrust efficiency is dependent strongly on the chemical model because the frozen-flow loss is generally one of the major losses in arcjets. In addition, the calculated radiative loss is found to be very small in Table 2, and commonly less than a few percent of the input power in all of the cases. From this standpoint, the contribution of radiation to the entire heat loss is investigated more accurately in the following section.

Radiation Analysis

Radiation Model

The two-temperature assumption is also introduced to the radiation analysis. Local thermal equilibrium is assumed to determine the population of excited states according to the Boltzmann distribution. The plasma is assumed to be optically thin as a result of the small dimension of the arc column.

Bound–bound radiation of the atomic and molecular species is computed by the line-by-line method.[14] Ignoring the fine structures, hydrogen atoms are made to populate 40 electronic levels according to the Boltzmann distribution, and 780 corresponding transitions are incorporated. On the other hand, nine electronic levels of molecular hydrogen are taken into account, and molecules are distributed among the electronic–rotational–vibrational levels in the similar manner of Ref. 14. Two prominent band spectra, namely the Lyman ($B^1\Sigma_u^+ \leftrightarrow X^1\Sigma_g^+$) and Werner ($C^1\Pi_u \leftrightarrow X^1\Sigma_g^+$) systems, are taken into consideration. Free–bound and free–free radiation are com-

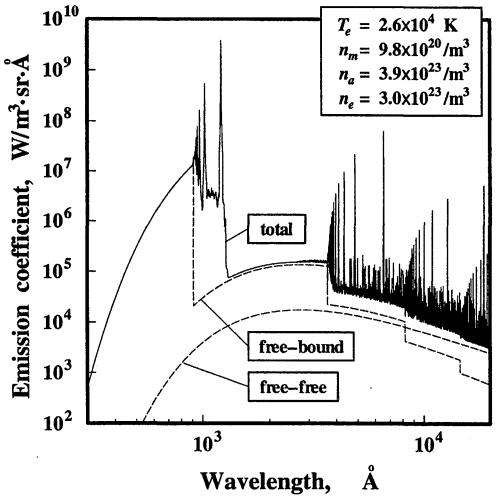

Fig. 8 Emission coefficient at the constrictor middle on the center axis for $\dot{m}$ = 10 mg/s and I = 15 A.

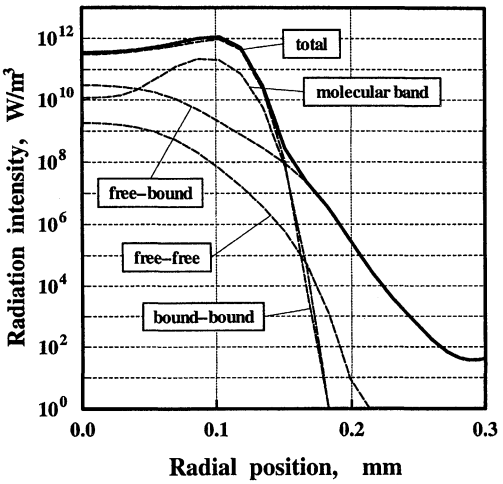

Fig. 9 Radial profile of radiation intensity for $\dot{m}$ = 10 mg/s and I = 15 A.

puted with the corresponding Gaunt factors evaluated by assuming a Maxwellian distribution for the electron thermal velocity.

Results

In the following results, the radiative loss is calculated in a noncoupled manner, using the temperature and density results obtained by the flow computation. Figure 8 shows a typical spectrum of the emission coefficient at the middle of the constrictor on the center axis for $\dot{m}$ = 10 mg/s and I = 15 A. A strong bound-free continuum is found in the ultraviolet region, where the wavelength is shorter than 912.3 Å, followed by the Werner band and the Lyman series with much higher intensity. Although free–free radiation becomes superior to free-bound radiation in the infrared region, the former is much smaller than the latter as a whole.

The total radiation intensity is evaluated by integrating the spectral intensity over wavelengths from 10^2 to 10^6 Å. Figure 9 shows the radial change of the total intensity at the middle of the constrictor for $\dot{m}$ = 10 mg/s and I = 15 A. The atomic bound–bound radiation is the most intense of all, whereas free–free radiation is negligible. Because the majority of the radiative energy is emitted from the arc column because of its high temperature, bound–bound radiation is considered to be the largest component of the total radiative loss. Net radiation decreases drastically in the range $r > 0.12$ mm, where the electron temperature decreases below 12,000 K. This is because the bound–bound radiation is more strongly dependent on the electronic excitation temperature rather than the number density.

Table 3 Radiative loss for $\dot{m}$ = 20 mg/s and I = 10 A

Radiation process	% of calculated IV
Atomic free–free	<0.1
Atomic free–bound	1.1
Atomic bound–bound	10.9
Molecular band	2.8

The net radiative loss from the entire plasma is estimated as shown in Table 3. Because self-absorption is not taken into consideration in the present analysis, the radiative loss is overestimated to some extent, and a conclusion obtained from these results is only a possibility that the radiative heat transfer is not explicitly negligible in the arc column. However, provided that the absorption is not significant because of the small dimension of the constrictor region, the radiative loss is thought of as one of the chief energy losses from the arc column. Taking account of this effect, distributions of physical properties may be significantly influenced. Therefore, to predict thruster performance more accurately, it might be necessary to take the radiation process into consideration even in low-power operation.

Conclusions

A detailed arcjet model has been developed and applied to performance prediction of a low-power hydrogen arcjet. The model takes account of chemical and thermal nonequilibria (two-temperature model), Ohmic heating, and the electrode sheath. Calculation results for the IRS ARTUS-4 arcjet show good agreement with experiment. With current and propellant flow rate given as the operating parameters, discharge voltages are calculated within 15% error. However, the model overestimates the specific impulse by 5–15%, which correspondingly deflects the calculated thrust efficiencies from experimental values.

An accurate radiation analysis has been made to account for the performance overprediction of the numerical model. Results show that bound–bound radiation, which becomes significant as the electron temperature exceeds 12,000 K, is most responsible for the radiative loss, and contributes to the total energy loss as well. To predict arcjet performance accurately, it may be necessary to take account of the radiative heat transfer, even in low-power operation.

References

[1]Smith, R. D., Yano, S. E., Armbruster, K., Roberts, C. R., Lichtin, D. A., and Beck, J. W., "Flight Qualification of a 1.8 kW Hydrazine Arcjet System," 23rd International Electric Propulsion Conf., Paper 93-007, Sept. 1993.

[2]Messerschmid, E. W., Zube, D. M., Kurtz, H. L., and Meinzer, K., "Development and Utilization Objectives of a Low-Power Arcjet for the P3-D (OSCAR) Satellite," 23rd International Electric Propulsion Conf., Paper 93-056, Sept. 1993.

[3]Sutton, A. M., Bromaghim, D. R., and Johnson, L. K., "Electric Propulsion Space Experiment (ESEX) Flight Qualification & Operations," AIAA Paper 95-2503, July 1995.

[4]Butler, G. W., Kull, A. E., and King, K. Q., "Numerical Simulations of Hydrogen Arcjet Performance," 23rd International Electric Propulsion Conf., Paper 93-249, Sept. 1993.

[5]Rhodes, R. and Keefer, D., "Non-Equilibrium Modeling of Hydrogen Arcjet Thrusters," 23rd International Electric Propulsion Conf., Paper 93-217, Sept. 1993.

[6]Miller, S. A., and Martinez-Sanchez, M., "Two-Fluid Nonequilibrium Simulation of Hydrogen Arcjet Thrusters," *Journal of Propulsion and Power*, Vol. 12, No. 1, 1996, pp. 112–119.

[7]Megli, T. W., Lu, J., Krier, H., and Burton, R. L., "Modeling Plasma Processes in 1-Kilowatt Hydrazine Arcjet Thrusters," *Journal*

of Propulsion and Power, Vol. 14, No. 1, 1998, pp. 29–36.

[8]Riehle, M., Auweter-Kurtz, M., and Kurtz, H., "High Specific Impulse Experiments with 1.5- and 5-kW Thermal Arcjets," 23rd International Electric Propulsion Conf., Paper 93-210, Sept. 1993.

[9]Fujita, K., "Performance Computation of a Low-Power Hydrogen Arcjet," AIAA Paper 96-3183, July 1996.

[10]Smithells, C. J., *Metals Reference Book*, 5th ed., Butterworths, London, 1976.

[11]Fujita, K., "Arc Column Behavior and Heat Loss Mechanism in a DC Arcjet Thruster," Ph.D. Dissertation, Dept. of Aeronautics and Astronautics, Univ. of Tokyo, Japan, Feb. 1995.

[12]Yee, H. C., "Construction of Explicit and Implicit Symmetric TVD Schemes and Their Applications," *Journal of Computational Physics*, Vol. 68, No. 1, 1987, pp. 151–179.

[13]Obayashi, S., Matsushima, K., Fujii, K., and Kuwahara, K., "Improvements in Efficiency and Reliability for Navier-Stokes Computations Using the LU-ADI Factorization Algorithm," AIAA Paper 86-0338, Jan. 1986.

[14]Arnold, J. O., Whiting, E. E., and Lyle, G. C., "Line by Line Calculation of Spectra from Diatomic Molecules and Atoms Assuming a Voigt Line Profile," *Journal of Quantitative Spectroscopy and Radiative Transfer*, Vol. 9, No. 6, 1969, pp. 775–798.